Soil Dynamics and Earthquake Engineering 30 (2010) 1430–1445

Contents lists available at ScienceDirect

Soil Dynamics and Earthquake Engineering

journal homepage: www.elsevier.com/locate/soildyn

Interaction of foundation–structure systems with seismically precarious slopes: Numerical analysis with strain softening constitutive model

R. Kourkoulis, I. Anastasopoulos, F. Gelagoti, G. Gazetas *

National Technical University of Athens, Greece

ARTICLE INFO

Article history:
Received 18 November 2009
Received in revised form
28 April 2010
Accepted 1 May 2010

ABSTRACT

This paper studies the combined effects of earthquake-triggered landslides and ground shaking on foundation–structure systems founded near slope crests. Plane-strain nonlinear finite element dynamic analyses are performed. The soil constitutive model is calibrated against published data to simulate the (post-peak) softening behavior of soil during a seismic event and under the action of gravitational forces. The plastic shear zones and the yield accelerations obtained from our dynamic analyses are shown to be consistent with the slip surfaces and the seismic coefficients obtained by classical pseudostatic limiting equilibrium and limit analysis methods. The foundation and frame columns and beams are modeled as flexural beam elements, while the possibility of sliding and detachment (separation) between the foundation and the underlying soil is considered through the use of special frictional gap elements. The effects of foundation type (isolated footings versus a rigid raft) on the position of the sliding surface, on the foundation total and differential displacements, and on the distress of the foundation slab and superstructure columns, are explored parametrically. It is shown that a frame structure founded on a properly designed raft could survive the combined effects of slope failure and ground shaking, even if the latter is the result of a strong base excitation amplified by the soil layer and slope topography.

© 2010 Elsevier Ltd. All rights reserved.

1. Introduction

The seismic bearing capacity of shallow footings on top of slopes has been studied mostly with pseudostatic limit equilibrium methods, which impose the inertia of soil mass in a simplified way [56,55,6,79]. Such studies have produced diagrams for assessing the reduction in bearing capacity as the foundation gets closer to the crest. But evidently, limit equilibrium methods would only very crudely simulate soil–structure interaction effects during earthquake shaking. This is especially the case with soils that degrade with increasing number of cycles, such as those examined in the present study. On the other hand, the decrease of strength from its peak to the residual value, leading to progressive soil failure, is dealt in the limiting equilibrium method in a conservative simplified way [70,60,80]. To simulate progressive soil-failure and shear-zone development, finite element analyses have been in use for more than 30 years (e.g. [24,31,13,40,49,32,74,51].

While all the above studies were performed for static or pseudo-static conditions, the present study is dynamic, based on non-linear finite element modeling with a post-peak softening material law. The potential separation of the foundation from the soil, due either to separation (uplift) or to the downward slope movement during landslide, is properly taken into account. The analysis can capture (with reasonable engineering realism) the mechanism of progressive slope failure and the influence of the presence of the foundation on the path of the generated failure zone. The soil is assumed to be dry, and pore pressure build up due to cyclic loading is not modeled.

2. Analysis of slope stability: overview

Numerous methods have been developed for assessing the stability of soil slopes, most of which are based on the concept of ideally plastic response when failure is imminent. Among them, the *limit equilibrium* methods enjoy wide acceptance due to their reasonable agreement with reality and their simplicity [17,8,26,41,64]. Complex soil profiles, seepage, and a variety of loading conditions can be easily dealt with [77]. Limit equilibrium solutions, however, are not rigorous. To be called rigorous, a solution must satisfy the equilibrium equations, the compatibility conditions, the constitutive relations of all materials, and the boundary conditions. Limit equilibrium methods often violate the stress boundary conditions, they do not enforce an appropriate plastic flow rule for the soil, while the developing stresses may not everywhere obey the requirement for non-exceedance of soil strength. Moreover, the introduction of assumptions

* Corresponding author.
E-mail address: gazetas@ath.forthnet.gr (G. Gazetas).

0267-7261/$ - see front matter © 2010 Elsevier Ltd. All rights reserved.
doi:10.1016/j.soildyn.2010.05.001

necessary to remove static indeterminacy leads to kinematically inadmissible collapse mechanisms.

On the other hand, *limit analysis* models the soil as a perfectly plastic material obeying an associative flow rule. If the normality condition is applied to a frictional soil with a friction angle φ, it is implied that large volume expansion occurs during plastic flow. Frictional soils are found experimentally to dilate considerably less than predicted by the normality condition: hence real soils do not follow the associative flow rule [6]. However, in slope stability, lateral earth pressure, and bearing capacity problems, deformation conditions are not so restrictive and the actual soil deformation properties do not affect the collapse load significantly. Hence, it is reasonable to utilize the limit analysis with the associated flow rule for the analysis of slope stability. Drescher and Detournay [14] and Michalowski [38] have extended the applicability of the method to soils with non-associated flow rule.

The limit-analysis solution is bounded according to the *upper-bound* and *lower-bound* theorems [15,11,81]. These are rigorous solutions only in the sense that either the "*stress*" field associated with a lower-bound solution is in equilibrium with the imposed loads at the boundaries, or the "*velocity*" field associated with an upper-bound solution is compatible with imposed "velocities". Lower-bound solutions satisfy equilibrium; upper-bound solutions provide collapse mechanisms. The (usually small) discrepancy between upper-bound and lower-bound solutions provides a built-in error check on the accuracy of the approximate collapse load [77].

Due to the complexity in construction of proper stress and velocity fields and in obtaining the optimal solutions, the method of limit analysis has not prevailed. Moreover, it is not computationally straightforward to include effects such as the existence of pore water pressures, soil inhomogeneity, and irregular slope geometry. Recently, however, finite-element-based methods for calculating upper bound solution of slopes with multilayered or irregularly deposited soil profiles have been developed [82,83].

The finite element (FE) method is an alternative approach employed with two different methodologies: (a) those that search for the critical slip surface using stress fields obtained from the stress and deformation FE analysis ; and (b) those that compute the factor of safety through an iterative finite element analysis, by the '*strength reduction technique*' [78,35,22,24,31,40,50,49,13,32,74,51].

In the latter category of methods, finite elements are utilized to model the development of shear zones and the progressive failure of soil. The advantages of the FE approach over the conventional slope stability methods can be summarized as follows:

- No assumption needs to be made *a priori* about the shape and location of the slip surface. Failure occurs naturally within the soil when the applied shear stresses exceed the shear strength of the soil mass.
- The solution is kinematically admissible, and there are no arbitrary assumptions about the slice side forces.
- It can capture progressive failure phenomena, and provides information about the displacement field until the ultimate state.
- It can readily (if not easily) handle irregular slope geometries in 2 and 3 dimensions, complex soil stratigraphy, and calculation of flow quantities (due to steady seepage, or to transient flow).

Moving now to the seismic problem, it is noted that despite the advances in *static* slope stability analysis, in the realm of limit equilibrium methods *seismic* stability is still largely approached pseudo-statically. Notwithstanding the uncertainties in determining the required (single) horizontal acceleration, the pseudo-static approach is often inadequate to describe the behavior of soils that progressively lose their strength with increasing number of cycles and to account for the interplay of the deforming slope with structures on top of it.

In this paper, we propose a non-linear FE-analyses-based procedure for seismic analysis of a slope with a strain-softening soil. The constitutive relation is calibrated to realistically simulate the response of both clayey and sandy soils under cyclic loading. The sliding surface is not pre-defined but "emerges" naturally as a continuous shear band comprising soil elements that have reached or exceeded their peak shear strength.

3. Problem statement, numerical discretisation, steps of the analysis

The four problems parametrically studied herein are sketched in Fig. 1(a–d). They all refer to a 23° slope, 30 m high, consisting of post-peak softening sandy clay with the properties summarized directly in Fig. 1a. The total upslope thickness of this soil layer is 40 m and is underlain by a 20 m thick stiff sandy soil layer down to bedrock. While Fig. 1a refers to the free-field problem, i.e. of the slope without any structure affecting it, Fig. 1b–d examine the interaction of the precarious slope with a number of idealized structures not far from its crest:

- a rigid uniformly loaded raft foundation (Fig. 1b),
- a three-bay single-story frame on isolated footings (Fig. 1c),
- a similar frame founded on a rigid raft (Fig. 1d).

The horizontal base excitation is uniformly applied along the x-axis, utilizing a set of both real accelerograms and idealized mathematical pulses (Ricker wavelets). The selected time-histories cover a wide range of seismic motions, ranging from medium intensity records of relatively short duration (e.g. Kalamata, 1986; Pyrgos, 1993; Aegion, 1996; Monastiraki, 1999; Ricker 3, Ricker 1) to very strong accelerograms (e.g. Kobe, 1995 JMA and Takatori, Imperial Valley 1994) featuring a large number of significant cycles. In the following sections, results are shown only for two extremes (Fig. 2):

- Ricker 1 wavelet scaled at $A=0.82$ g; a narrow-band excitation of 1 Hz dominant frequency and total duration of 3.5 s, comprising one significant pulse, preceded and followed by two smaller pulses.
- The JMA record of the Kobe 1995 earthquake ($A=0.82$ g); a very strong seismic excitation from all points of view (amplitude, large-period content, number of significant cycles).

The Ricker wavelet is deliberately scaled at the same PGA (0.82 g) to allow for direct comparisons.

The general problem studied herein and the FE discretization is displayed in Fig. 3. Quadrilateral 4-noded plane-strain elements are utilized. To minimize undesired parasitic boundary effects and to persuasively simulate the free-field conditions at the lateral boundaries, the symmetric problem is considered where the nodes at the opposite vertical sides are forced to move simultaneously only in the horizontal direction, preventing any rotation. The model is subjected to plane vertically incident SV waves applied at the bedrock level (model base nodes).

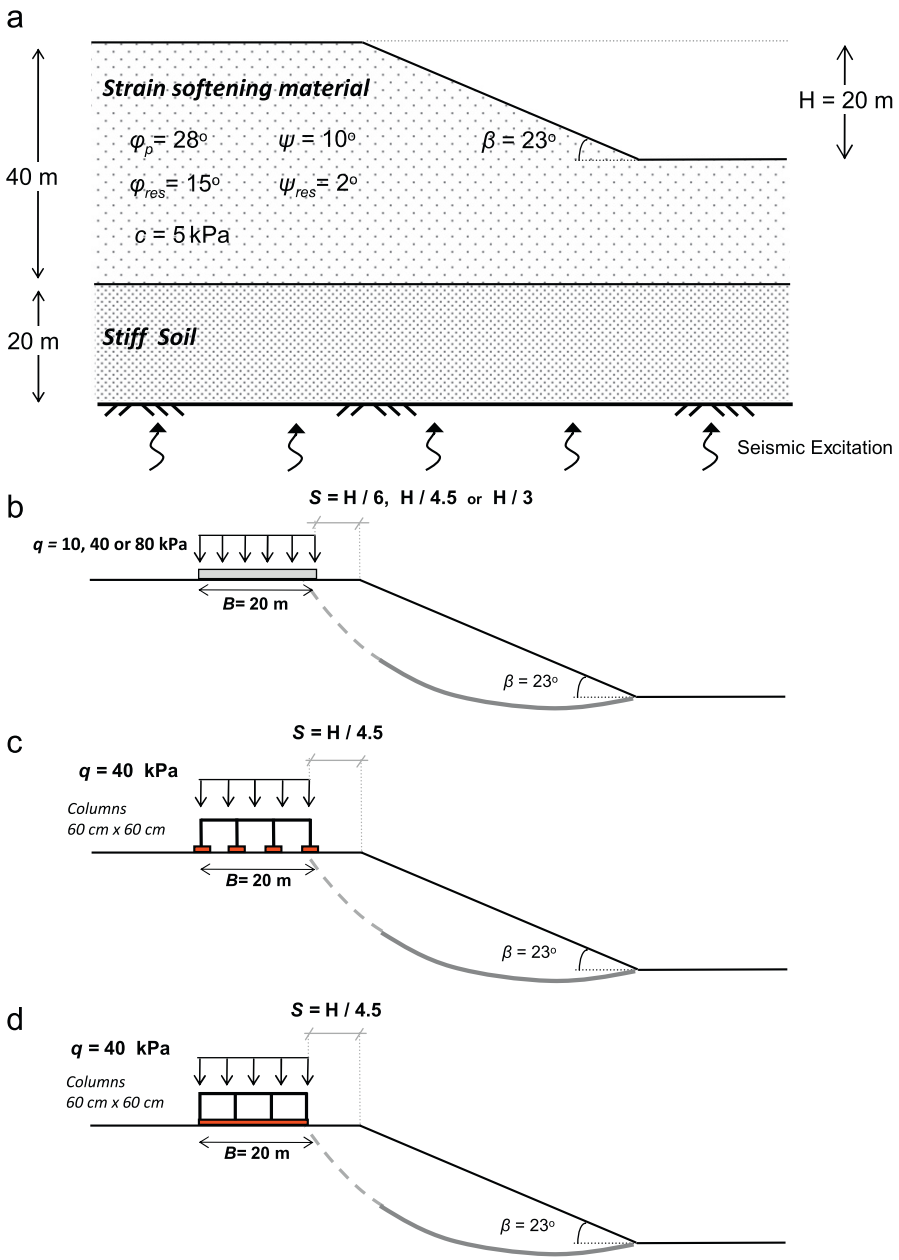

Fig. 1. Geometry and soil properties of the analyzed slope: (a) at the free-field, (b) with a rigid uniformly loaded slab foundation, (c) with a 3-bay single storey frame on isolated footings, and (d) with a 3-bay single storey frame on rigid raft.

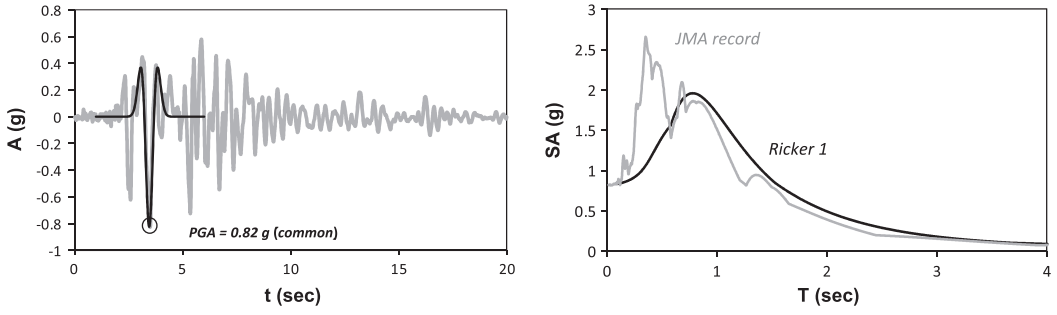

Fig. 2. The two seismic excitations discussed in the paper (Kobe JMA and Ricker 1), along with their 5% damped response acceleration spectra.

The fact that strain softening models may introduce mesh dependency phenomena produces further complications in generating a suitable FE mesh [46]. The importance of such phenomena has been explored through a detailed parametric study to determine the proper element size. The thickness of the produced shear zone was found to depend on the element size,

d_{FE}, of the FE grid. For $d_{FE} \leq 0.5$ m the location of the failure surface is not sensitive to mesh density. For the purpose of the present study, a discretization of 0.5 m × 0.5 m (in the area of the slope) has been adopted. Towards the lateral boundaries of the model (where the accuracy requirements loosen) the mesh is coarser: 2 m × 1 m. The use of finer mesh has no effect on the position of the concentrated plastic shear zone (which we may call 'failure' zone for brevity), while at the same time the computational time increases exponentially.

The numerical analysis is performed in three consecutive steps:

(1) *Gravity loading* (static analysis) establishment of the initial state of stress in the slope.
(2) *Seismic excitation* (dynamic analysis) triggering of shear band (depending on the intensity of seismic shaking, a shear band extending from toe to crest may develop, with plastic strains reaching or exceeding their peak-strength values, at least in a few locations).
(3) *Post-earthquake response* (analysis in the time domain) evolution of the seismically triggered landslide after the end of shaking due to the action of gravity (if a continuous shear-band has developed during seismic shaking and soil elements have reached their residual strength, deformations will keep increasing becoming, in principle, infinitely large).

4. Constitutive modeling of soil

The mechanism of progressive failure was recognized at an early stage of Soil Mechanics [70,84] while its crucial role in

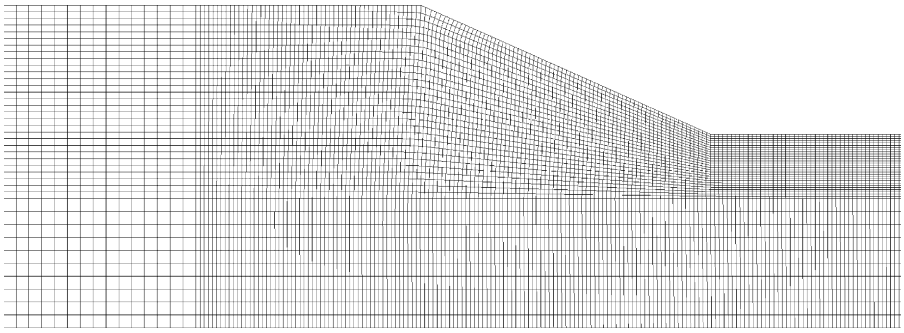

Fig. 3. Finite element mesh. In the area of the slope the discretizaton is denser (0.5 m × 0.5 m quadrilateral elements); towards the lateral boundaries the mesh is coarser. Elementary transmitting boundaries ensure insignificant contamination of the response with spurious wave reflections.

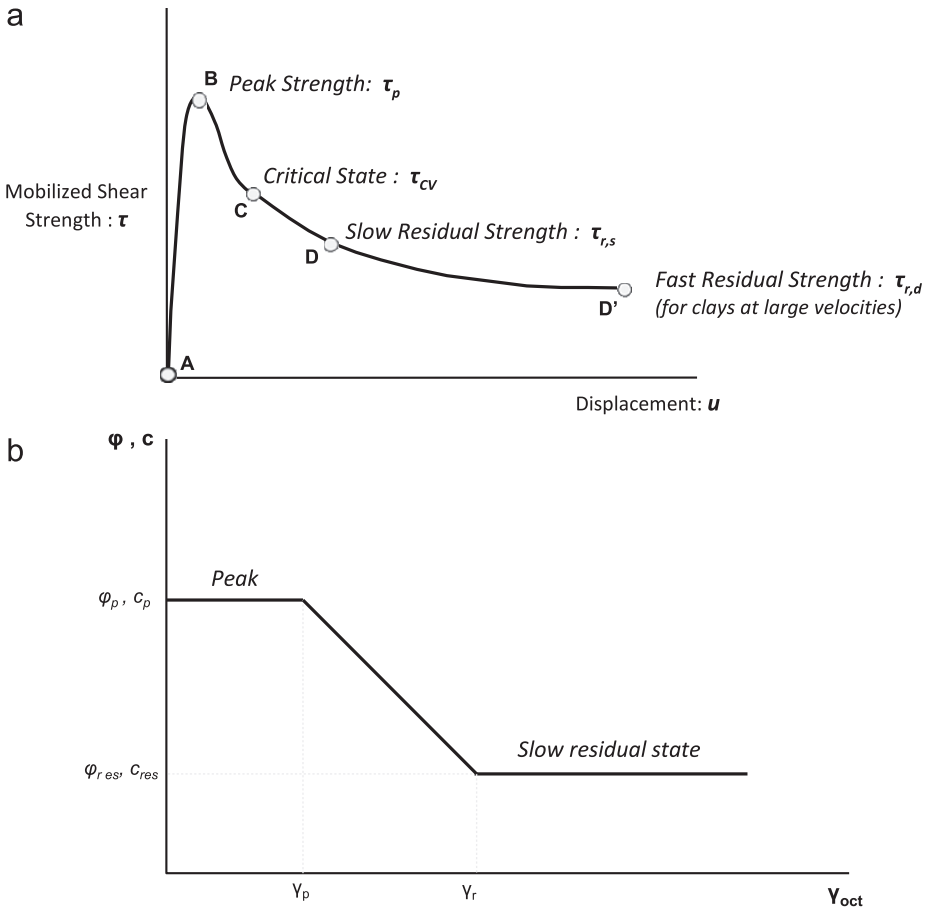

Fig. 4. (a) Idealized evolution of the mobilized shear band resistance during the sliding process. The following phases are identified: *Pre-shear-band behavior*: A–B–C, *Material softening*: C–D (adapted from [21]); (b) Idealized simulation of the strain softening behavior as encoded in ABAQUS.

stability problems was revealed by Skempton [60], Peck [44], and Turnbull and Hvorslev [75]. Progressive failure of soil occurs if it deforms non-uniformly. Then, as post-peak strains within the failure zone increase, the mobilized resistance reduces from peak towards residual. Final rupture of the soil mass usually takes place before the residual strength has developed everywhere. Thus, the average strength of the mass at failure is less than the peak strength of the soil and greater than the residual strength. Although complete numerical analyses with incorporating progressive failure were performed quite early [24], there are still relatively few pertinent examples in the literature [53,68,7,27,50,13].

The residual strength of clay has been studied extensively and numerous correlations between slow residual strength and index properties have been proposed (e.g. [33,61,10,72]). As shown schematically in Fig. 4a, soil behavior can be categorized in two distinguished phases [21]:

1. *Pre-shear-band behavior* (path A–B–C): The peak strength is mobilized at the very early stage of displacement, and then drops to the critical state, triggering the creation of a shear band.
2. *Material softening* (path C–D): The material inside the shear band is frictionally softened due to strain rate increase.

In this study we adopt an elastoplastic constitutive model with Mohr–Coulomb failure criterion, and isotropic strain softening properly calibrated in order to "macroscopically" imitate the previously described behavior of clay under shear loading. Pre-yield behavior (path A–B in Fig. 4a) is modeled as linear elastic, with a secant modulus $G_s=\tau_y/\gamma_y$ linearly increasing with depth. Post-peak material softening (path B–C–D or B–C–D′) is modeled through a reduction of the mobilized friction angle φ and dilation angle ψ with the increase of octahedral plastic shear strain. As shown in Fig. 4b, the model assumes a linear decrease of φ and ψ with increasing plastic octahedral shear strain to their slow residual state values, φ_{res} and ψ_{res}, respectively. The model is encoded in the FE numerical algorithm ABAQUS through a user subroutine. Model parameters are calibrated through direct shear test results, as described in Anastasopoulos et al. [5].

Despite its simplicity and (perhaps) lack of generality, the constitutive model employed herein is believed to capture adequately the predominant mode of deformation of the studied problem. The values utilized in the analyses discussed below are: $\varphi_{peak}=28^o$, $\varphi_{res}=15^\circ$, $\psi=10^o$, $\psi_{res}=0^\circ$, yield strain $\gamma_y=2\%$, and failure strain $\gamma_f=12\%$.

5. Validation of numerical analysis methodology

The numerical analysis methodology employed herein has been validated against limit equilibrium, limit analysis, and FE analysis results [29], for the case of mild homogeneous slopes susceptible to landsliding. This section illuminates the validity of the analysis methodology as to its ability to predict the slope failure surface and its critical seismic acceleration. The case studied refers to a well documented idealized homogeneous slope (Fig. 5a), which has been analyzed thoroughly by Loukidis et al. [32] through numerical (FE) limit analysis and widely accepted conventional (Bishop's and Spenser's) limit equilibrium methods (Fig. 5b).

In order to compare the published analytical results with the ones obtained by means of the dynamic analysis proposed here, the slope was dynamically excited using a variety of records as base excitations. Model boundaries were set at a sufficient distance to avoid contamination with spurious wave reflections. In case of moderate seismic shaking, no significant soil displacements were observed, consistent with the findings of other researchers [54]. With adequately strong seismic excitations, slope failure was triggered and a well-defined shear zone (or slip surface) developed. In this case, the soil mass overlying the failure surface starts sliding on it infinitely denoting total failure. As illustrated in Fig. 5c, the shape and position of the failure surface obtained by the analysis methodology compares satisfactorily with pseudo-static (numerical and limit equilibrium) analysis methods (Fig. 5b). The numerically predicted slip surface is understandably somewhat shallower than the pseudo-static slip surfaces, in reflection of the higher accelerations at the sloping surface (due to soil and topographic amplification) than inside the sloping soil mass—something that can only be captured through dynamic analysis (see Fig. 5c, and similar findings for slopes of earth dams in [18]). Various authors [54,3] indicate that slope topography may amplify the developed accelerations in such a mild slope by not more than 10%; however this factor rises considerably as the slope becomes steeper [2]. Such effects can only be captured by means of two-dimensional analyses.

In pseudo-static analysis terminology, the critical or yield acceleration (a_c) is defined as the acceleration which, when applied uniformly and pseudo-statically to a potentially sliding wedge, produces a state of incipient failure ($FS=1$). In a nonlinear dynamic analysis (such as the one of this paper), a_c can be obtained as the average of peak accelerations of soil elements within the sliding wedge. Higher *average* accelerations cannot be transmitted through the particular interface (slip surface). Isolated values, however, such as for example the crest acceleration, can be higher thanks to the unavoidable flexibility of the wedge [18,19]—definitely an important difference from the pseudo-static method. Hence, the resulting acceleration, $a_c \approx 0.46$

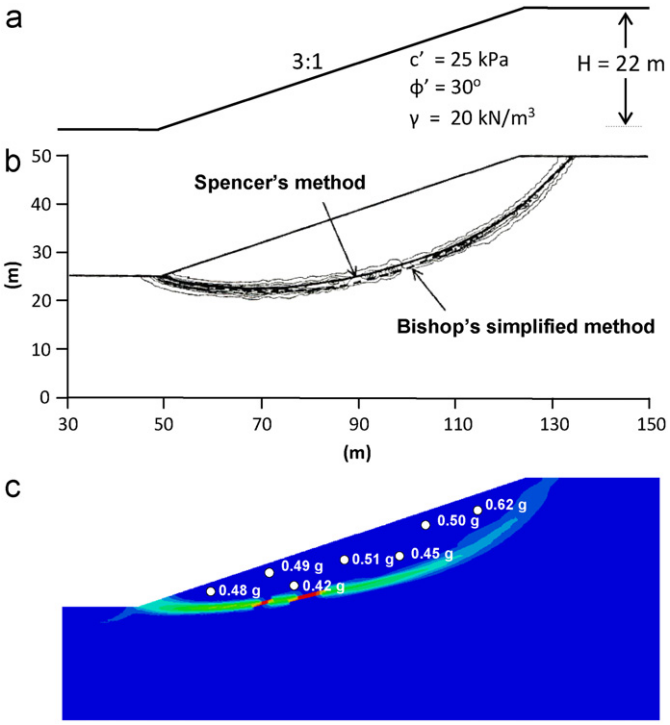

Fig. 5. Validation of the numerical analysis methodology against limit analysis and limit equilibrium results from the literature [32]: (a) Problem geometry, (b) Loukidis et al. [32] FE limit analysis failure surface compared with Bishop's and Spenser's limit equilibrium methods, and (c) failure surface predicted through the nonlinear *dynamic* FE analysis of this paper, along with maximum acceleration values at different points within the slope.

g is slightly higher than the values from the limiting equilibrium analysis (Spencer's method: 0.43 g, Bishop's: 0.42 g, Sarma's: 0.43 g) and quite similar to the numerical upper bound solution of 0.45 g reported by Loukidis et al. [32]. It should be noted that the analyses presented in the ensuing do not focus on the accurate prediction of the slope critical acceleration and failure surface location but rather on the effects of generalized, landslide-induced displacements on structures founded on the slope's crest.

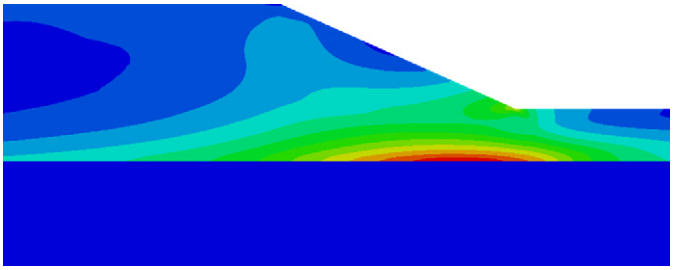

Fig. 6. Free-field dynamic analysis with the Ricker 1 wavelet at $A=0.82$ g: plastic strain contours upon completion of seismic shaking. Despite the exceedance of the pseudo-static yield acceleration ($ac \approx 0.2$ g), no shear band ("failure") mechanism develops.

6. Free-field dynamic analysis: development of failure surface

Before proceeding to the analysis of the interaction, we briefly discuss typical results for the free-field problem, i.e. the development of the failure (sliding) surface in the absence of a structure (Fig. 1a). Based on peak soil strength, limit equilibrium analysis yields a static safety factor $FS_{stat}=1.5$ for the slope investigated herein. Employing the c, φ reduction method and allowing for progressive decrease of the shear strength of some elements towards their residual value, FE static analysis predicts a somewhat lower $FS_{stat}=1.45$.

We first show the results for the Ricker 1 wavelet at $A=0.82$ g: a seismic motion substantially exceeding the pseudo-static yield acceleration of the investigated slope, $a_c=0.20$ g (as computed through finite element analysis employing the c, φ reduction method). Fig. 6 illustrates the distribution of plastic strains upon completion of seismic shaking. Some plastic strains have been generated, localized at the interface of the underlying stiff rock with the much softer overlying soil, but no slip surface (shear band) has developed. This is confirmed by the maximum horizontal displacement, which is of the order of few centimeters after completion of the "post-seismic" Step 3 (not shown herein for brevity), implying that the slope remains stable after the end of the earthquake. Evidently, although the imposed seismic excitation seriously exceeds the pseudo-static a_c of the

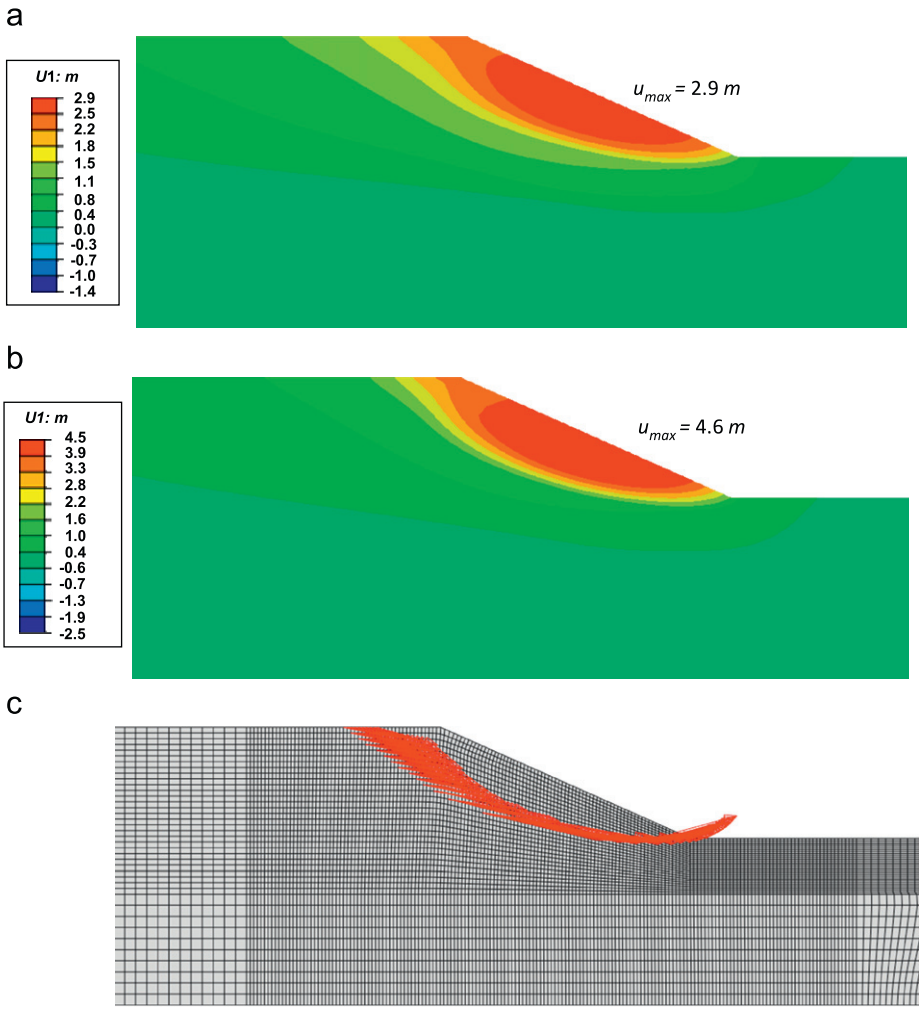

Fig. 7. Free-field dynamic analysis with the JMA record ($A=0.82$ g): Contours of horizontal displacement (a) upon completion of seismic shaking, and (b) post seismically (i.e. after completion of Step 3); (c) deformation vectors along the generated sliding surface at the end of seismic shaking.

slope, the single strong motion cycle of the Ricker wavelet is not enough to generate a sliding surface.

The response of the slope is totally different when subjected to the JMA record, which has the same PGA ($A=0.82$ g) but dramatically different frequency content and kinematic characteristics (sequence of strong motion cycles, etc.). As shown in Fig. 7a, at the end of seismic shaking (Step 2 of the analysis) the peak permanent horizontal displacement amounts to 2.9 m, increasing further to 4.6 m during the "post-seismic" Step 3. The magnitude of such displacements (of the order of meters) *and*

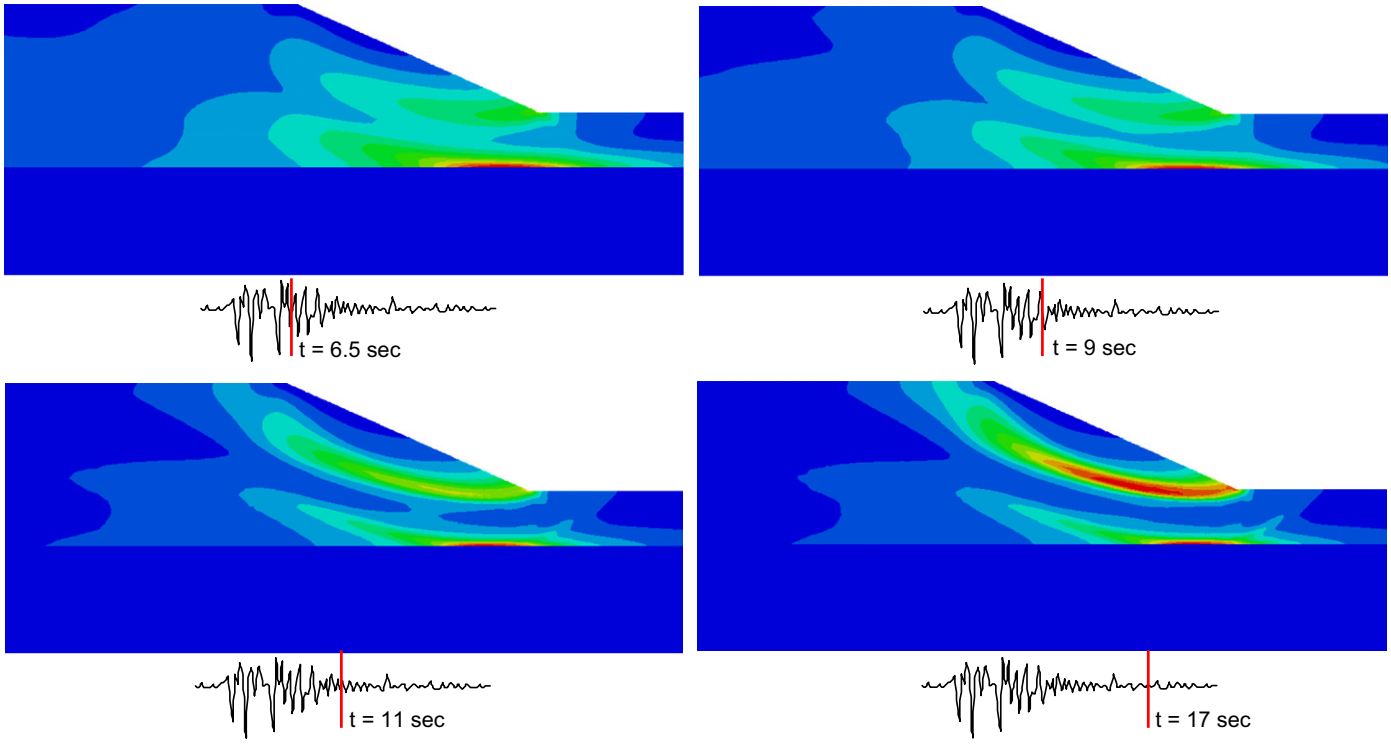

Fig. 8. Free-field dynamic analysis with the JMA record ($A=0.82$ g): evolution of plastic shear strains during seismic shaking.

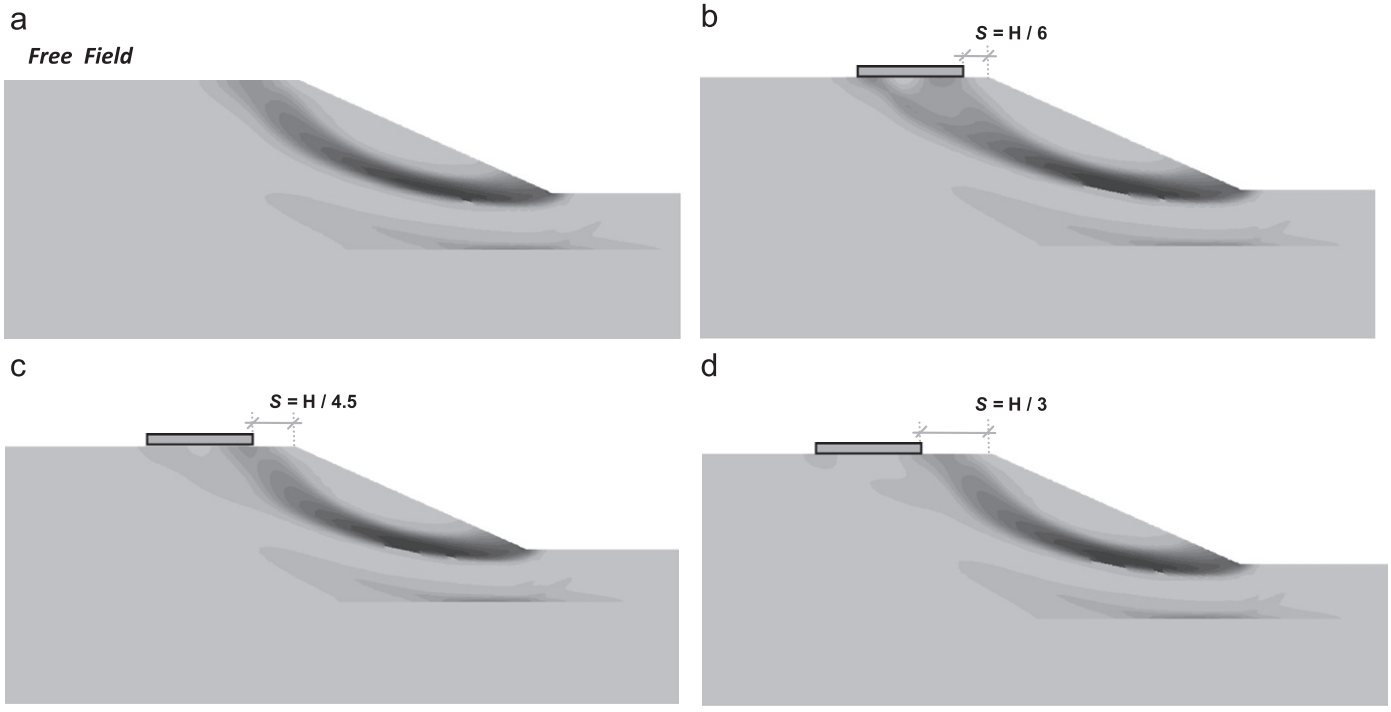

Fig. 9. Rigid $B=20$ m raft foundation with surcharge load $q=40$ kPa placed parametrically at $S=H/6$, $H/4.5$ and $H/3$ (Kobe JMA seismic excitation): distribution of seismically induced plastic shear strains at the end of seismic shaking (Step 3).

the fact that they keep increasing after the end of the earthquake (Step 3), clearly imply the development of a sliding surface. This is confirmed in Fig. 7c, in which we plot the deformation vectors along the sliding surface immediately after the completion of the seismic excitation. Fig. 8 depicts the evolution of the shear zone during seismic shaking. The failure zone initiates at the toe of the slope and propagates towards its crest. In contrast to the "weak" single-pulse Ricker 1 wavelet, the JMA record not only has managed to develop a continuous plastic shear localization, but since the slope continues to "slide" after the end of the earthquake, it has generated enough plastic strain to "drive" the elements belonging to the sliding surface to their residual post-peak (reduced) strength values.

Summarizing, it is quite interesting to note that although the PGA of the two excitations shown here was exactly the same, the response differs completely not only in terms of the produced displacements but also in terms of failure potential: while the Ricker wavelet is relatively harmless, the JMA record with its four or five strong-motion cycles triggers complete slope failure.

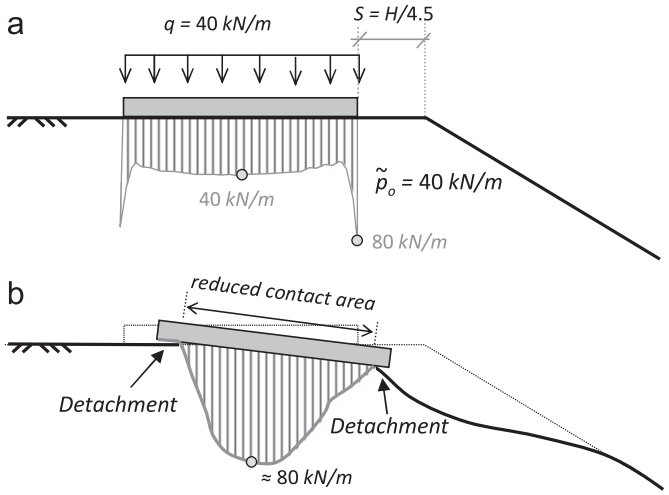

Fig. 10. Rigid $B=20$ m raft foundation with surcharge load $q=40$ kPa at distance $S=H/4.5$ from the slope crest (Kobe JMA seismic excitation): (a) static contact pressures and (b) contact pressures after the end of seismic shaking.

7. Soil–raft foundation interaction on a seismically failing slope

The interaction of a uniformly loaded raft foundation with the failing slope (as sketched in Fig. 1b) is investigated in the following section. Emphasis is placed on the consequences of seismic slope instability on the foundation, and conversely on the influence of the presence of the foundation to the behavior of the slope. Note that this is a different problem from the pseudo-static evaluation of bearing capacity of footings as a function of their proximity to the crest of the slope, which has been studied with limit equilibrium methods by Sarma and Chen [56] and Sawada et al. [58], and with upper-bound limit analysis by Askari and Farzaneh [6].

The FE analysis is conducted in four consecutive steps: (i) application of the self-weight of soil elements (i.e. geostatic loading); (ii) application of surcharge load q onto the foundation; (iii) seismic shaking; and (iv) post-seismic analysis in the time domain. Results are presented for the particular studied slope with $B=20$ m rigid foundation placed parametrically at a distance from the crest $S=H/6$, $H/4.5$, $H/3$, where H is the height of the slope. The uniform surcharge load is also parametrically investigated: $q=20$, 40, and 80 kPa. In all cases discussed in the sequel, we focus on the JMA record which is enough to trigger slope instability.

7.1. The effect of foundation location

Fig. 9 portrays the distribution of the seismically induced plastic shear strains for the foundation loaded with $q=40$ kPa and placed at different locations S relative to the crest of the slope. The response of the free field (slope without structure) is also documented to allow immediate comparison. The following trends are worthy of note:

(a) When the footing is located relatively close to the crest (at distance $S=H/6$), the generated shear band ("failure" surface) shifts its path from its original free-field position towards the

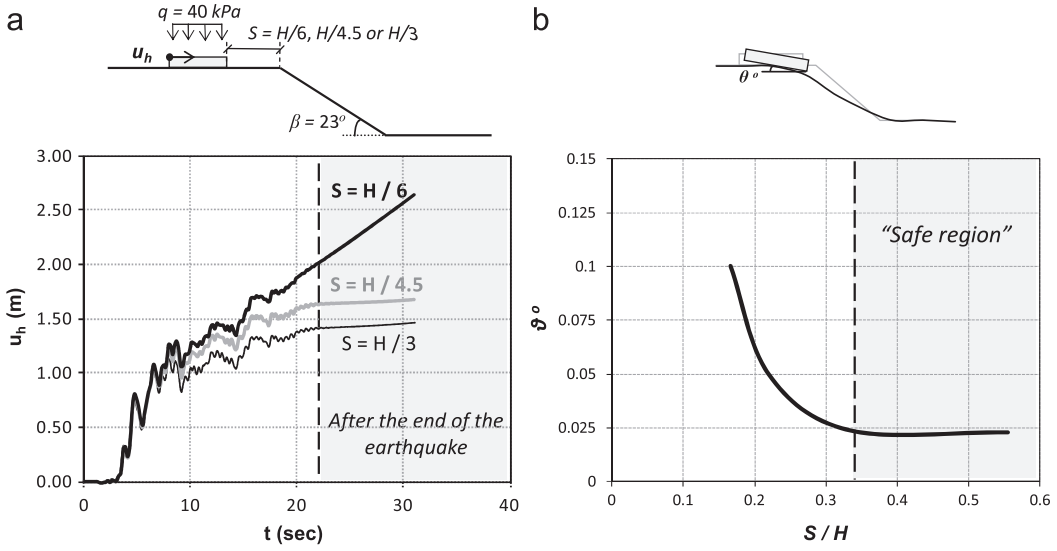

Fig. 11. Rigid $B=20$ m raft foundation with surcharge load $q=40$ kPa (Kobe JMA seismic excitation) placed parametrically at different locations relative to the crest of the slope: (a) time-history of horizontal displacement u_h of the foundation; and (b) foundation rotation θ as a function of its normalized distance S/H from the slope crest.

inner part of the slope, outcropping on the left edge of the footing; a secondary plastic zone emerges at the right edge of the foundation. Apparently, in this case a bearing capacity type failure mechanism is partially activated due to limited support of the foundation from the downhill sliding wedge. As a result, the foundation rotates extensively. To yield a better picture, in Fig. 10 we plot the distribution of contact pressures underneath the foundation. The top figure (Fig. 10a) plots the distribution of static contact pressures, followed below (Fig. 10b) by the contact pressures after completion of seismic shaking (end of Step 3). The change is quite substantial, accompanied by a reduction in the effective contact area of the raft: detachment of foundation from the bearing soil at the two edges. The time history of horizontal displacement u_h of the foundation (Fig. 11a) reveals nonzero horizontal velocity at the end of seismic shaking, implying

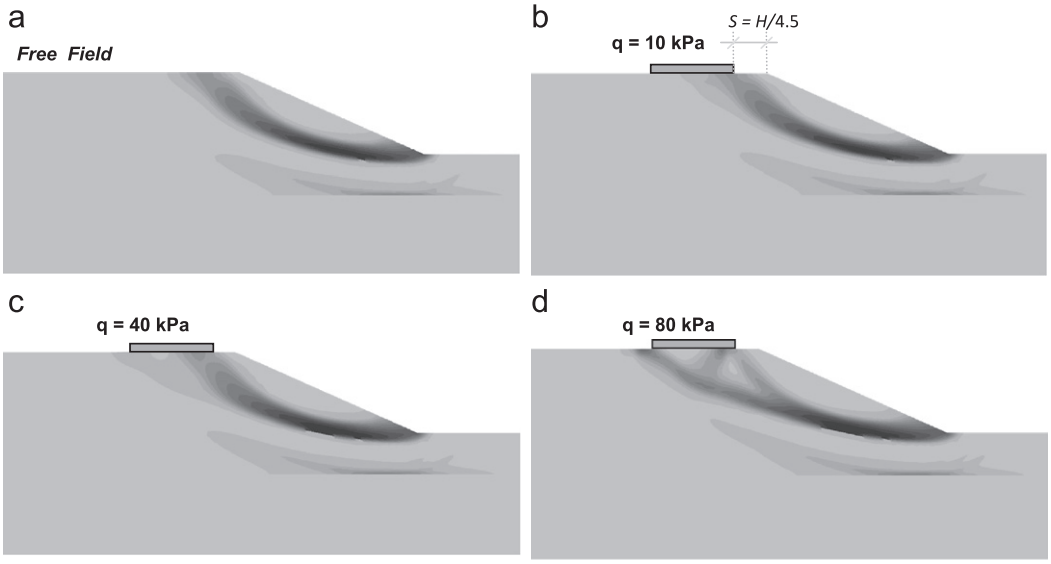

Fig. 12. Rigid $B=20$ m raft foundation placed at $S=H/4.5$ with parametrically varied surcharge load q (Kobe JMA seismic excitation): distribution of seismically induced plastic shear strains at the end of seismic shaking (Step 3).

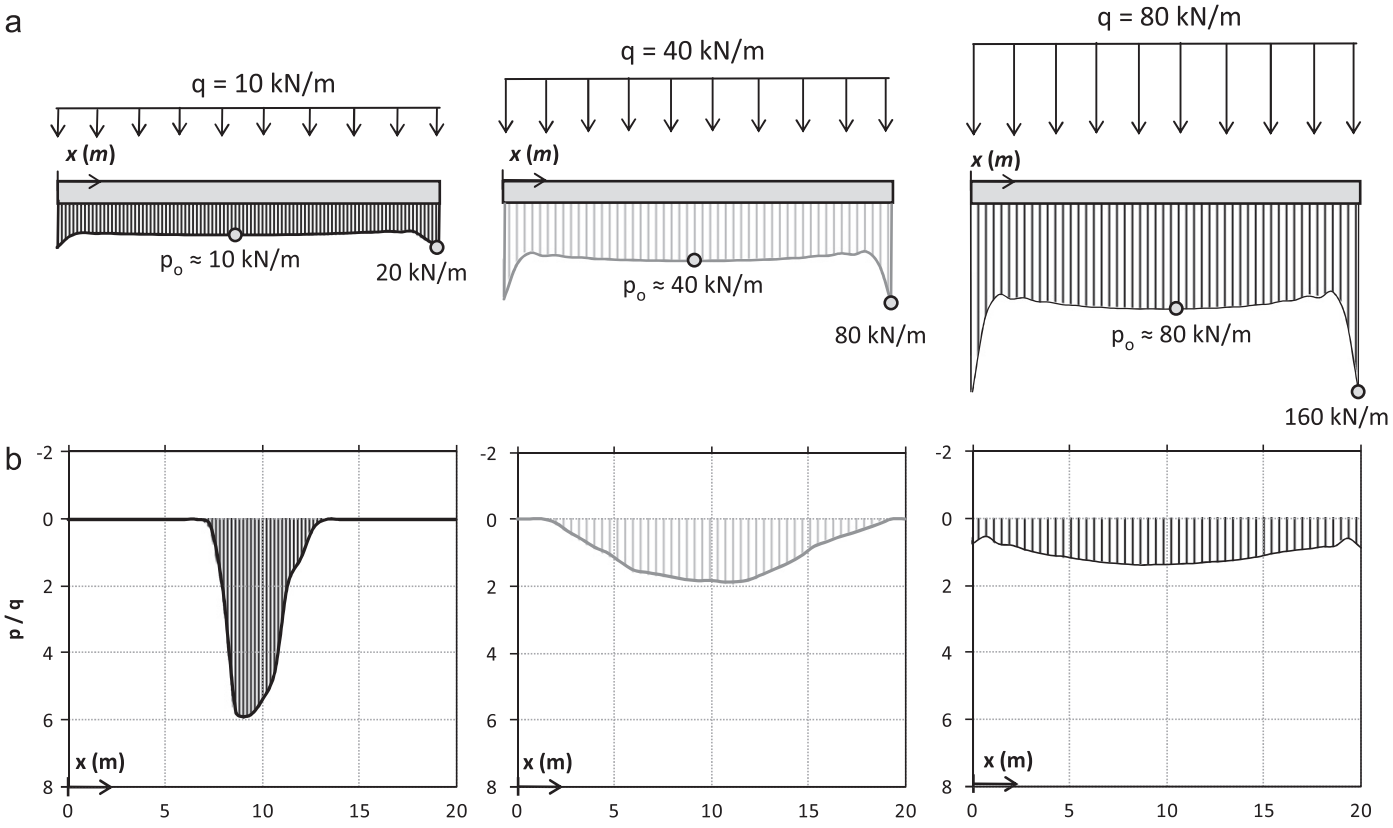

Fig. 13. Rigid $B=20$ m raft foundation placed at $S=H/4.5$ with parametrically varied surcharge load q (Kobe JMA seismic excitation). Distribution of contact pressures underneath the footing: (a) before seismic shaking (i.e. initial static contact pressures), and (b) after the end of seismic shaking (end of Step 3). In the latter case, the contact pressure p is normalized with the surcharge load q.

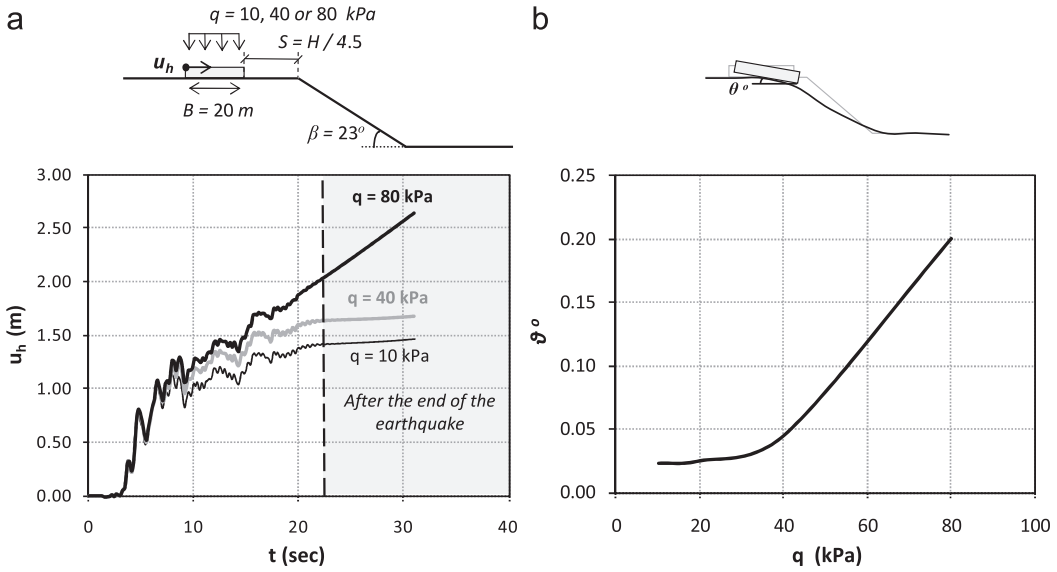

Fig. 14. Rigid $B=20$ m raft foundation placed at $S=H/4.5$ with parametrically varied surcharge load q (Kobe JMA seismic excitation): (a) time-history of horizontal displacement u_h of the foundation; and (b) foundation rotation θ as a function of the surcharge load q.

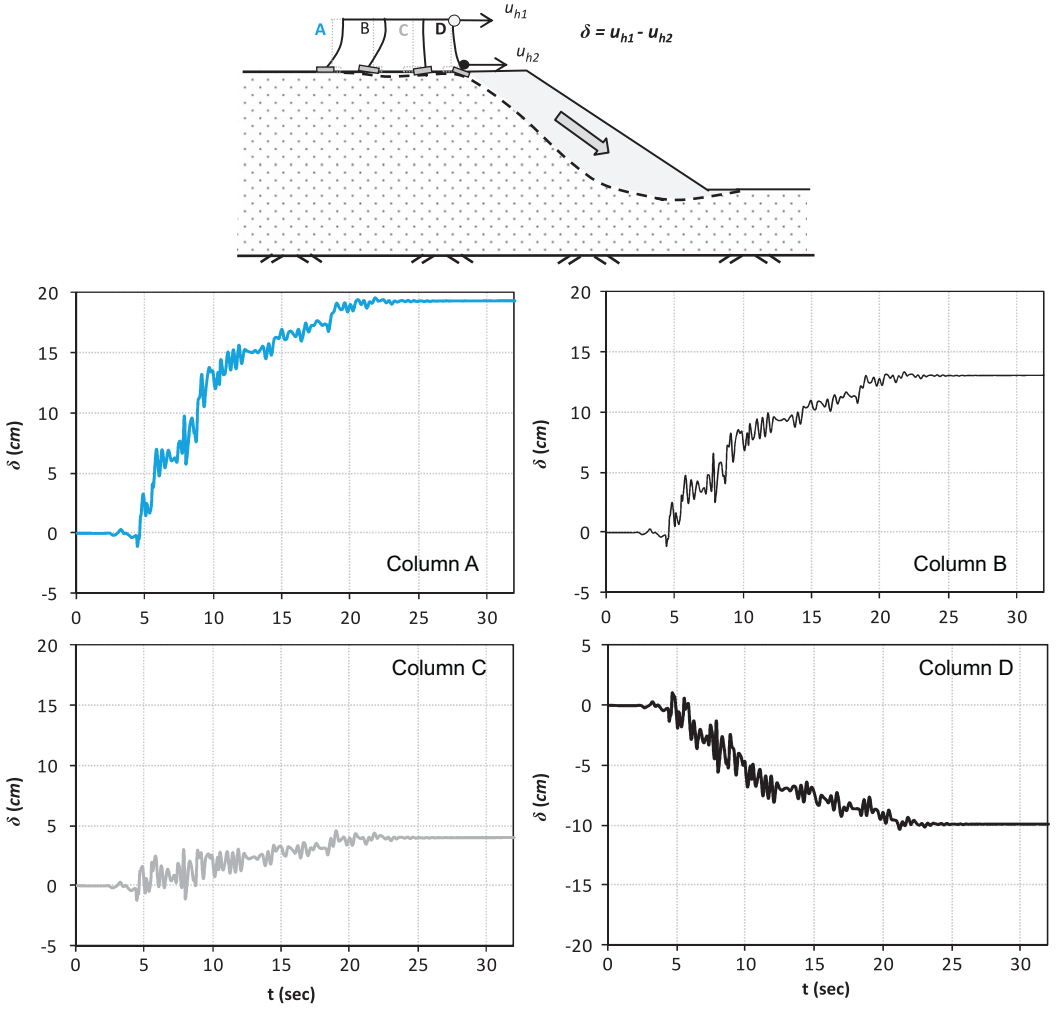

Fig. 15. Typical $B=20$ m moment resisting frame founded on isolated footings, at distance $S=H/4.5$ (Kobe JMA seismic excitation): time histories of interstorey drift δ developing in the four columns of the frame.

that the downhill sliding continues after the end of the earthquake. As it would be expected, the rotation θ of the foundation is increased with the decrease of its distance from the crest of the slope (Fig. 11b).

(b) Moving the footing farther from the crest ($S=H/4.5$), the generated shear zone becomes diffused and deviates slightly towards the foundation slab, which again loses contact from the underlying soil at both edges. The separation is largest under the crest side of the foundation, which now (perhaps as a beneficial result of this detachment) "survives" the landslide (i.e., no further displacement takes place (Fig. 11a)). This result is reminiscent of the response of a foundation over a rupturing normal fault (Anastasopoulos et al., 2008).

(c) When the distance of the foundation from crest increases even more ($S \geq H/3$ for $q=40$ kPa) the footing is located on a "safe region". In such a case, the existence of the structure hardly modifies the plastic shear strain field (see Fig. 9d), and failure occurs just beyond the right (closer to the slope) edge of the foundation, which never loses contact with the underlying soil.

7.2. The effect of surcharge load

Figs. 12–14 illustrate the significance of increasing the surcharge load q applied on the raft, for the worst-case location $S=H/4.5$. Results are displayed for a raft foundation of width $B=20$ m. The ultimate load of this foundation located on level ground is calculated according to Meyerhof [36] as $p_{ult}=2340$ kPa, while the FE calculation (as expected) overestimates this value by 17%. For sloping ground conditions, the ultimate load of the foundation may be reduced by a factor ranging from 1.5 to 2 depending on slope geometry and the distance of the foundation to the crest [56,6]. The FE analyses confirm these theoretical expectations. The loads applied on the footing vary between 20 and 80 kPa, i.e. the Safety Factor for all the footings examined is of the order of 10, so that bearing capacity failure be definitely avoided and the effects of landslide induced displacements be illuminated. Fig. 12 portrays the contours of plastic shear strain at the end of seismic shaking; Fig. 13 shows the changes in the distribution of foundation contact pressures p due to the seismically induced slope instability; and Fig. 14 shows the evolution in time of horizontal foundation displacement and the dependence of foundation response on q. The following remarks are worth noting:

(a) Increasing q from 20 to 80 kPa gives rise to a diversion of the zone of excessive shearing deformation (Fig. 12). This deviation of the path of the shear band is particularly conspicuous for $q=80$ kPa (Fig. 12d), in which case the shearing due to shaking of the slope "interacts" with the rudimentary bearing capacity mechanism under the footing (local shearing).

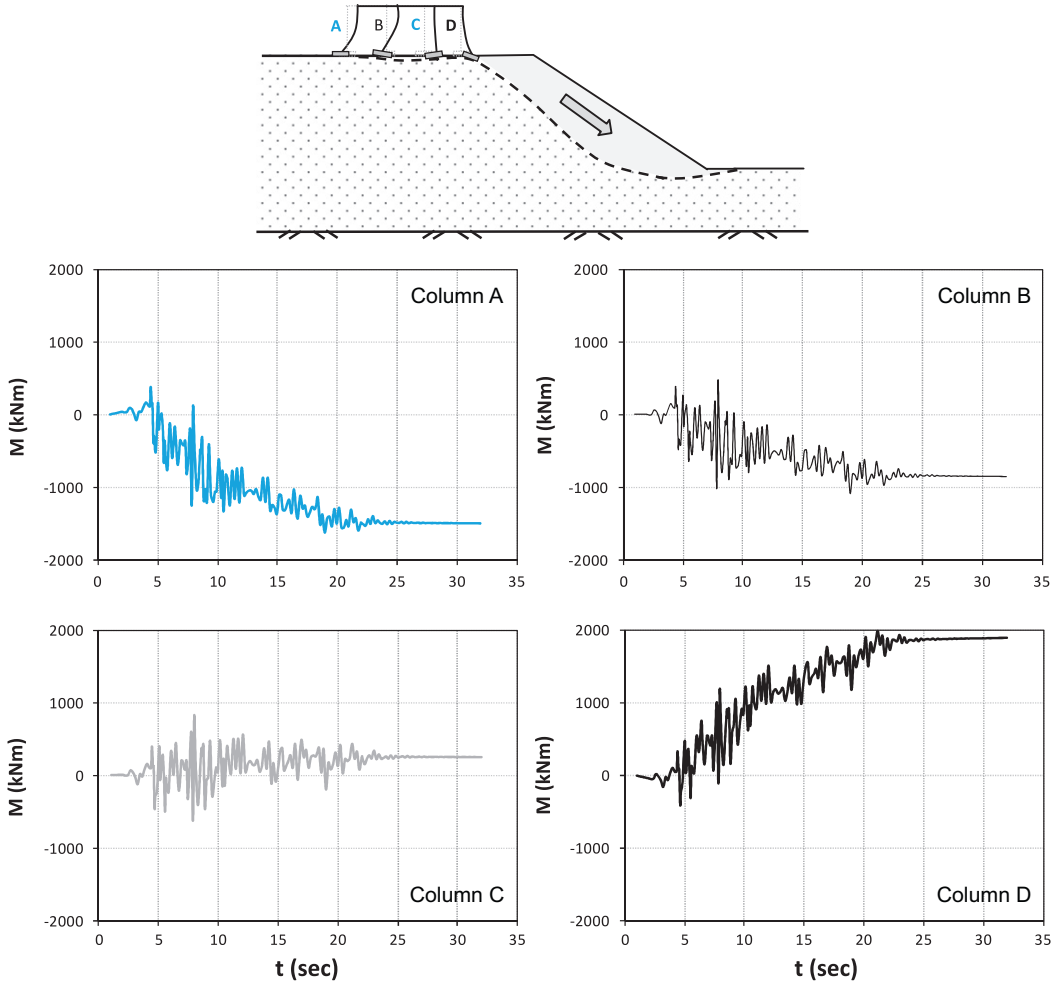

Fig. 16. Typical $B=20$ m moment resisting frame founded on isolated footings, at distance $S=H/4.5$ (Kobe JMA seismic excitation): time histories of bending moments M developing in the four columns of the frame.

(b) The foundation detachment from the supporting soil due to seismically induced slope instability that was observed with the light surcharge load ($q=20$ kPa) is diminished with the heavier load ($q=40$ kPa), practically disappearing for $q=80$ kPa (Fig. 13). Note that the remarkably large detachment of the lightly loaded foundation (only its middle 1/4 remains in contact) will generate huge bending moments on the raft.

(c) Fig. 14a reveals that the heavily loaded foundation is not safe: it has positive velocity at the end of shaking, and its displacement (outward and downward) continues to grow under the sole action of gravity (Step 4). Foundation rotation θ increases markedly with q (Fig. 14b).

8. Soil–frame interaction on a seismically failing slope

This section analyzes, a typical 3-span, 20 m wide and 3 m-high, reinforced-concrete moment-resisting frame, consisting of 0.60 m × 0.60 m columns, founded: (a) on 1.5 m wide isolated footings, and (b) on a 1 m thick raft foundation (see Fig. 1c and d). Emphasis is placed on the consequences of the structural inertia forces in conjunction with the imminent seismic slope instability on the distress of the foundation and the superstructure.

All structural components are modeled as elastic beam elements. Connection of the foundation nodes with the nodes of the soil is accomplished through suitable *friction-and-gap* elements to simulate the possibility of sliding and/or detachment (loss of contact) at the interface. Emphasis is given not on the absolute values of the internal forces in the structure, but on comparing the additional structural distress (due to inertial or kinematic loading) between the two foundation systems. Thus, the amplitude of the internal forces (M, Q, N) developed, may in some cases exceed the corresponding ultimate capacity of the structural component.

As for the previous cases, results are presented for Kobe 1995 JMA record, which is capable of generating slope instability. Recall that the Ricker 1 (i.e. $f_0=1$ Hz) excitation, with its small duration and practically 1 strong-motion cycle, was not sufficient to trigger slope failure even with PGA=0.82 g. Figs. 15 and 16 highlight the response of the frame on isolated footings, whereas Figs. 17 and 18 highlight the response of the same frame on the rigid raft. As already expected from the discussion of Fig. 9, the zone of excessive soil straining is hardly affected by the presence of the structure at this distance from the crest ($S=H/4.5$).

8.1. Distress of the superstructure: isolated footings

When the imposed shaking is not adequate to activate sliding of the soil mass, stressing of the structure is originating mainly by

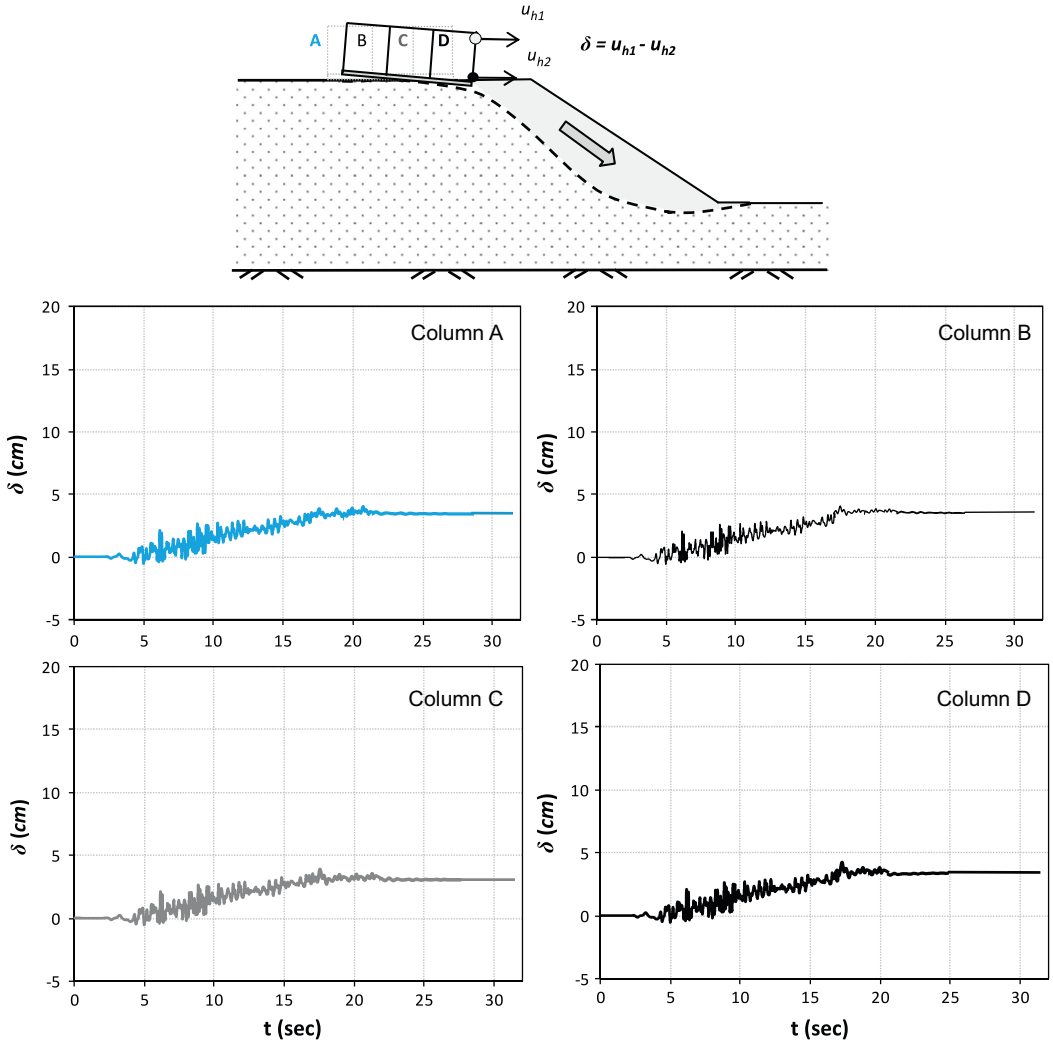

Fig. 17. Typical $B=20$ m moment resisting frame founded on a rigid raft foundation, at distance $S=H/4.5$ (Kobe JMA seismic excitation): time histories of interstorey drift δ developing in the four columns of the frame.

its inertial response. As previously discussed, for the slope geometry and properties examined here, the JMA record triggers the failure of the slope and consequently sparks off additional kinematic loading on the structure founded atop the slope. It is worth noting that 2D wave propagation effects, perhaps leading to "topographic" amplification, are taken into account in our analysis. It has been shown by numerous researchers that such effects may lead to increased amplitude of ground shaking near the crest of the slope. See, for example, Aki [1], Gazetas et al. [20], Pitilakis [47], Assimaki et al. [4], Ktenidou et al. [30], and Pitilakis [48].

Figs. 15 and 16 display the response of the structure in terms of interstorey drift (δ) and bending moment (M) time histories for all four frame columns. The most excessive drift ($\delta \approx 19$ cm) is experienced by the outer (more distant from the crest) column A whose footing displaces less than its top. The picture is qualitatively similar for column B, but with smaller drift ($\delta \approx 13$ cm). The drift of column C is merely $\delta \approx 4$ cm, and of column D ($\delta \approx 10$ cm) but in the opposite direction. Results for the developing bending moments show a similar trend, with columns A and D developing residual moments $M \approx 1600$ and 2000 kNm, respectively. Both δ and M can be seen to consist of two components: an oscillatory (cyclic) component, and a permanent (cumulative) component. The first is related to the inertial response of the soil–structure system, while the latter is the result of differential foundation displacements due to the downward movement of the failing slope.

It is noted that at time $t=22$ s, the whole acceleration time history has been applied to the model and the only acting force for the rest of the analysis (i.e. until $t=32$ s) is gravity. The flattening of the displacement versus time curve is representative of zero velocity of the structure nodes after the end of seismic shaking (Step 3), implying that the structure has not been dragged down by the landslide.

A caveat is appropriate here. The absolute values of the reported moments and deformations are an outcome of elastic analysis: by no means do they compare with the likely ultimate moment capacity of the columns! Such magnitudes of internal forces and deformations would certainly signify failure, bearing in mind that the ultimate moment of such a column, even if heavily reinforced, could hardly exceed about 1000 kNm. This implies that isolated footings are an inappropriate foundation solution for structures in the vicinity of potentially unstable slopes, even if they are not dragged downslope.

8.2. Distress of superstructure: raft foundation

Figs. 17 and 18 display the response of the structure founded on a rigid slab foundation in terms of horizontal drift δ and bending moment M time histories for all four columns of the frame. The picture is totally different in terms of both deformations and bending moments. The drift (Fig. 17), which is now the same for all columns since they are supported on a

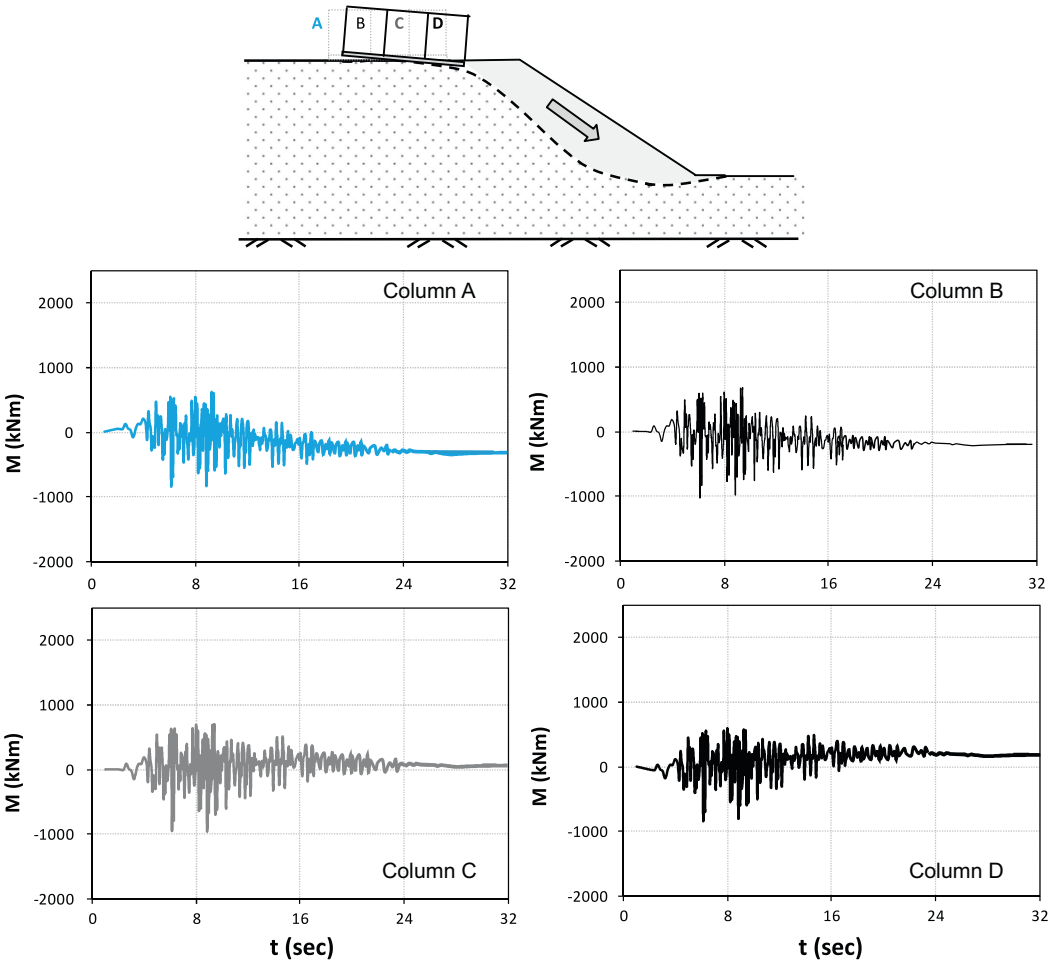

Fig. 18. Typical $B=20$ m moment resisting frame founded on a rigid raft foundation, at distance $S=H/4.5$ (Kobe JMA seismic excitation): time histories of bending moments M developing in the four columns of the frame.

common rigid foundation, does not exceed $\delta \approx 3$ cm despite the severity of ground shaking: the deformation-related cumulative component has practically disappeared. Similarly, the peak bending moments (Fig. 18) remain below the likely ultimate moment capacity of the columns, while their residual value is practically zero. Evidently, such deformation is mainly the result of ground shaking (“inertial” effect) and not of slope-induced deformation (“kinematic” effect).

The small magnitude of the distress of the columns (compared to the previous case) is attributed to the rigid-body movement of the structure, thanks to the rigidity and continuity of the foundation slab. The penalty, however, is the increased rotation and horizontal displacement of the structure as a whole. The rotation of the slab ultimately results in detachment from the underlying soil at both foundation edges. The areas of zero contact pressure observed in Fig. 19b denote the formation of a gap between the soil and the foundation after the end of ground shaking. Consequently, the whole structure is supported through a reduced effective width, equaling about 75% of the original width B. This results in a substantial increase of contact pressures (Fig. 19b) and foundation bending moments (Fig. 19c), compared to the static case (i.e. before the earthquake).

Fig. 20 plots the evolution of normalized contact pressures p/q (where q is the static contact pressure) underneath the footing at three characteristic locations: at the two edges (nodes A and B), and at the middle of the foundation (node C). Zeroing of the p/q denotes loss of contact between the footing and the ground. While at the middle of the foundation (node C) support is maintained through the whole duration of seismic shaking, while substantial loss of support can be observed at the two edges (nodes A and B). Note that once the failure surface has outcropped underneath the foundation, the right edge (node B) permanently detaches from the sliding soil wedge (due to its sliding displacement) resulting in rigid-body rotation of the footing and subsequently to its loss of support at the left edge (node A). Despite the unavoidable generation of increased internal forces on the foundation, it can safely be concluded that with proper design of the foundation structural safety can be ensured. A warning, however, is appropriate: before generalizing the above conclusions a more extensive parametric investigation must be performed to further explore the influence of slab flexibility, structure position, rigidity, strength and type of soil, and so on.

9. Conclusions

A numerical methodology has been presented for analyzing the performance of isolated and raft foundations carrying either a uniform surcharge load or a moment-resisting frame, when they are located near the crest of slopes, precarious to earthquake-triggered landslides.

A key conclusion of the study is that finite-element (FE) analyses can be successfully utilized to model the generation of sliding failure surfaces in the slope, reproducing similar failure

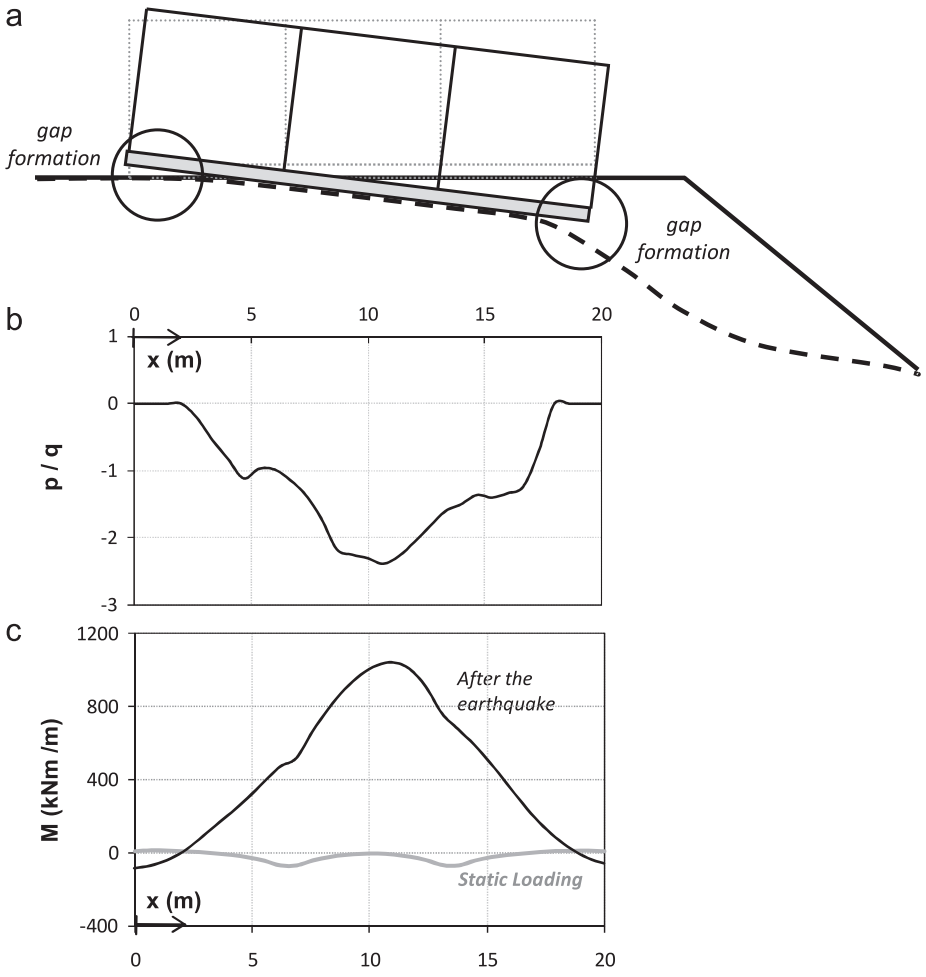

Fig. 19. Typical $B=20$ m moment resisting frame founded on a rigid raft foundation, at distance $S=H/4.5$ (Kobe JMA seismic excitation): (a) sketch elucidating the mechanism of gap formation underneath the rigid foundation slab; (b) normalized contact pressures p/q after the end of seismic shaking; and (c) foundation bending moments before (grey line) and after the end of the earthquake (solid black line).

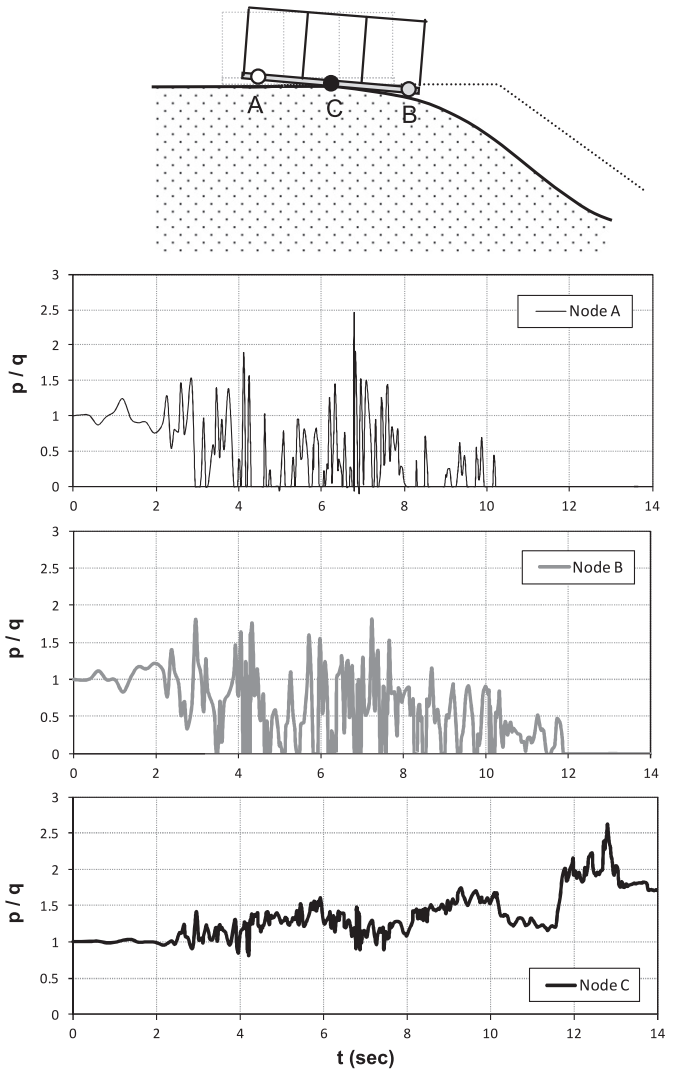

Fig. 20. Evolution of normalized foundation contact pressures p/q (where q is the static contact pressure) at three characteristic locations.

surfaces with those derived from venerable limit-equilibrium and limit-analysis methods, and leading to similar yield accelerations. But the capability to treat realistically the dynamic response to ground shaking is an exclusive attribute of the numerical (FE) methodology—not of the pseudostatic limit equilibrium/analysis methods.

An additional capability of the numerical (FE) methodology is that any structure-foundation system can be placed on top of the slope. As a result, we studied the interplay between dynamic (“inertial”) effects arising from the ground vibration and the quasi-static (“kinematic”) effects arising from the downward movement of a shallow sliding soil wedge. It was thus determined that a rigid raft foundation, even if located at a small distance (of the order of $H/4$) from the crest of a slope which is in a precarious equilibrium and fails during very strong shaking, can protect the superstructure from both falling (being dragged) with the sliding soil mass *and* from suffering large damaging internal forces. This is in qualitative agreement with several case histories of structures that have survived the combined effects of strong seismic shaking and of soil downward sliding. The penalty to pay, however, is: (a) appreciable rotation and lateral displacement of the whole system which may impair the serviceability of the structure, and (b) generation of large bending moments and shear forces in the foundation slab.

By contrast, as in fact most engineers would have intuitively predicted, placing a structure with isolated footings close to a seismically unstable slope would not be a prudent decision.

Acknowledgements

This work forms part of an EU 7th Framework research project funded through the European Research Council’s Programme “Ideas”, Support for Frontier Research – Advanced Grant, under Contract no. ERC-2008-AdG 228254-DARE.

References

[1] Aki K. Local site effects on strong ground motions, Earthquake Engineering and Soil Dynamics II. In: ASCE specialty conference, 1988, p. 103–55.
[2] Ashford SA, Sitar N. Analysis of topographic amplification of inclined shear waves in a steep coastal bluff. Bulletin of the Seismological Society of America 1997;87(3):692–700.
[3] Ashford SA, Sitar N. Simplified method for evaluating seismic stability of steep slopes. *Journal of Geotechnical and Geoenvironmental Engineering*, ASCE 2002;128(2):119–28.
[4] Assimaki D, Gazetas G, Kausel E. Effects of local soil conditions on the topographic aggravation of ground motion. Bulletin of the Seismological Society of America 2005;95(3):1059–89.
[5] Anastasopoulos I, Gazetas G, Bransby MF, Davies MCR, El Nahas A. Fault rupture propagation through sand: finite element analysis and validation through centrifuge experiments. *Journal of Geotechnical and Geoenvironmental Engineering*, ASCE 2007;133(GT 8):943–58.
[6] Askari F, Farzaneh O. Upper-bound solution for seismic bearing capacity of shallow foundations near slopes. Geotechnique 2003;53(8):697–702.
[7] Biondi P, Manfredini F, Martinetti S, Rickbackhi R Riccioni R.. Limit load of a foundation in a strain softening soil. In: Proceedings of the 2nd international conference on numerical methods in geomechanics, vol. 1, 1976, p. 591–6.
[8] Bishop AW. The use of the slip circle in the stability analysis of slopes. Geotechnique 1955;5(1):7–17.
[10] Bromhead EN, Curtis RD. A comparison of alternative methods of measuring the residual strength of London Clay. Ground Engineering 1983;16.
[11] Chen WF. Limit analysis and soil plasticity. Amsterdam: Elsevier Publishers; 1975.
[13] Dounias GT, Potts DM, Vaughan PR. The shear strength of soils containing undulating shear zones – a numerical study. Canadian Geotechnical Journal 1988;25:550–8.
[14] Drescher A, Detournay E. Limit load in translational failure mechanisms for associative and non-associative materials. Geotechnique 1993;43:443–6.
[15] Drucker DC, Prager W. Soil mechanics and plastic analysis or limit design. Quarterly of Applied Mathematics 1952;10(2):157–75.
[17] Fellenius W. Calculation of the stability of earth dams. Transactions of the 2nd congress on large dams, Washington, DC, vol. 4, 1936, p. 445–59.
[18] Gazetas G, Dakoulas P. Seismic analysis and design of rockfill dams: state-of-the art. Journal of Soil Dynamics and Earthquake Engineering 1992;11:27–61.
[19] Gazetas G, Uddin N. Permanent deformation on pre-existing sliding surfaces in dams. *Journal of Geotechnical Engineering,* ASCE 1994;120(11): 2041–2061.
[20] Gazetas G, Kallou PV, Psarropoulos PN. Topography and soil effects in the Ms 5.9 Parnitha (Athens) earthquake: the case of Adames. Natural Hazards 2002;27(1-2):133–69.
[21] Gerolymos N, Vardoulakis I, Gazetas G. A thermo-poro-visco-plastic shear band model for seismic triggering and evolution of catastrophic landslides. Soils and Foundations 2007;47(1):11–25.
[22] Griffiths DV, Lane PA. Slope stability analysis by finite elements. Geotechnique 1999;49(3):387–403.
[24] Hoeg K. Finite element analysis of strain softening clay. Journal of the Soil Mechanics and Foundations Division, ASCE 1972:43–59.
[26] Janbu N. Earth pressures and bearing capacity calculations by generalised procedure of slices. In: Proceedings of the 4th international conference on soil mechanics and foundation engineering, London, vol. 2, 1957, p. 207–12.
[27] Kalteziotis, NA, Kyrou, K. Undrained bearing capacity of strain softening clay. In: Proceedings of the 11th international conference on soil mechanics, San Francisco, vol. 2, 1985, p. 773–6.
[29] Kourkoulis R. Interplay of mat foundations and piles with a failing slope. PhD thesis, National Technical University of Athens, Greece, 2009.
[30] Ktenidou, OJ, Raptakis, D, Pitilakis, K, Chávez-García FJ. Engineering aspects of site and topography effects at Aegion, Greece. In: Gazetas G, Goto Y, Tazoh T, editors. Proceedings of the 3rd Greece–Japan workshop seismic design, observation, and retrofit of foundations, Santorini, 2009, p. 495–505.
[31] Lo KY, Lee CE. Stress analysis and slope stability in strain softening materials. Geotechnique 1973;23(1):1–11.
[32] Loukidis D, Bandini P, Salgado R. Stability of seismically loaded slopes using limit analysis. Geotechnique 2003;53(5):463–79.
[33] Lupini JF, Skinner AE, Vaughan PR. The drained residual strength of cohesive soils. Geotechnique 1981;31(2):181–213.

[35] Matsui T, San KC. Finite element slope stability analysis by shear strength reduction technique. Soils and Foundations 1992;32:59–70.
[36] Meyerhof, GG. The bearing capacity of foundations under eccentric and inclined loads. In: Proceedings of the 3rd international conference on soil mechanics and foundation engineering, Zurich, vol. 1, 1953, p. 440–5.
[38] Michalowski RL. Slope stability analysis: a kinematic approach'. Geotechnique 1995;45(2):283–93.
[40] Modaressi, H, Aubry D, Faccioli, E Noret, C. Numerical modelling approaches for the analysis of the earthquake triggered landslides. In: Prakash S, editor. Proceedings of the 3rd international conference on recent advances in geotechnical earthquake engineering and soil dynamics, St. Louis, MO, vol II, 1995, p. 833–43.
[41] Morgenstern N, Price VE. The analysis of the stability of general slip surfaces. Geotechnique 1965;15(1):79–93.
[44] Peck RB. Stability of natural slope. *Journal of Soil Mechanics and Foundations Division,* ASCE 1967;93:403–36.
[46] Pietruszezak S, Mroz Z. Finite element analysis of deformation of strain softening material. International Journal of Numerical Methods in Engineering 1981;17(3):327.
[47] Pitilakis K. Site effects. In: Ansal A, editor. recent advances in geotechnical earthquake engineering and microzonation. Kluwer Academic; 2004. p. 139–98. Chapter 5.
[48] Pitilakis D. Topographic irregularities and soil–foundation–structure interaction. In: Gazetas G, Goto Y, Tazoh T, editors, Proceedings of the 3rd Greece–Japan workshop seismic design, observation, and retrofit of foundations, Santorini, 2009, p. 335–43.
[49] Potts DM, Kovacevic N, Vaughan PR. Delayed collapse of cut slopes in stiff clay. Geotechnique 1997;47(5):953–82.
[50] Potts DM, Dounias GT, Vaughan PR. Finite element analysis of progressive failure of Carsington embankment. Geotechnique 1990;40(1):79–101.
[51] Pradel D, Smith PM, Stewart JP, Raad G. Case history of landslide movement during the nothridge earthquake. *Journal of Geotechnical and Geoenvironmental Engineering,* ASCE 2005;11:1360–9.
[53] Prevost JH, Hoeg K. Soil mechanics and plasticity analysis of strain softening. Geotechnique 1975;25(3):279–97.
[54] Rathje EM, Bray JD. One- and two-dimensional seismic analysis of solid-waste landfills. Canadian Geotechnical Journal 2001;38(4):850–62.
[55] Sarma SK, Iossifelis IS. Seismic bearing capacity factors of shallow strip footings. Geotechnique 1990;40(2):265–73.
[56] Sarma SK, Chen YC. Bearing capacity of strip footings near sloping ground during earthquakes. Proceedings of the 11th world conference on earthquake engineering, Acapulco, 1996.
[58] Sawada T, Nomachi SG, Chen WF. Seismic bearing capacity of a mounded foundation near a down-hill slope by pseudo-static analysis. Soils and Foundations 1994;34(1):11–7.
[60] Skempton AW. Long term stability of clay slopes. Geotechnique 1964;14(2):77–101.
[61] Skempton AW. Slope stability of cuttings in brown London Clay. In: Proceedings of the 9th international conference on soil mechanics and foundation engineering, San Francisco, vol. 3, 1985, p. 261–70.
[64] Spencer E. A method of analysis of the stability of embankments assuming parallel interslice forces. Geotechnique 1967;17(1):11–26.
[68] Sture S, Ko HY. Stress analysis of strain softening clay. In: Proceedings of the 2nd international conference on numerical methods in geomechanics, vol. 1, 1976, p. 580–9.
[70] Terzaghi K, Peck RB. Soil mechanics in engineering practice, 1st ed.. New York: Wiley; 1948.
[72] Tika ThE, Hutchinson JN. Ring shear tests on soil from the Vaiont landslide slip surface. Geotechnique 1999;49(1):59–74.
[74] Troncone A. Numerical analysis of a landslide in soils with strain-softening behaviour. Geotechnique 2005;55(8):585–96.
[75] Turnbull WJ, Hvorslev MJ. Special problems in slope stability. Journal of Soil Mechanics and Foundation Engineering, ASCE 1967;93(SM4):499–528.
[77] Yu HS, Salgado R, Sloan SW, Kim JM. Limit analysis versus limit equilibrium for slope stability. Journal of Geotechnical Engineering, ASCE 1998;124(1):1–11.
[78] Zienkiewicz OC, Humpheson C, Lewis RW. Associated and non-associated viscoplasticity and plasticity in soil mechanics. Geotechnique 1975;25:671–89.
[79] Kumar J, Rao VBKM. Seismic bearing capacity factors for spread foundations. Géotechnique 2002;52(2):79–88.
[80] Bjerrum L. Progressive failure in slopes of over consolidated plastic clays and clay shales. I. Jour. Soil Mech. Fdn. Div., ASCE, 1967, p. 93–349.
[81] Davis RO, Selvadurai APS. Elasticity and geomechanics. Cambridge University Press, New York (2002).
[82] Chuang PH. Stability analysis in geomechanics by linear programming, part I–II, J. Geotech. Eng., 118, 1992, p. 1696–726.
[83] Jiang GL, Magnan JP. Stability analysis of embankments: comparison of limit analysis with method of slices. Géotechnique 1997;47(4):857–72.
[84] Taylor DW, (1948), Fundamentals of soil mechanics. New York: Wiley, 700 p.